Prototype studies on the forward MWDC tracking array of the external target experiment at HIRFL-CSR *

YI Han (易晗)[1] ZHANG Zhao(张钊)[1] XIAO Zhi-Gang(肖志刚)[1,3;1)] CHENG Wen-Jing(程文静)[1]
LÜ Li-Ming(吕黎明)[1] YAN Wei-Hua(闫威华)[1] WANG Ren-Sheng(王仁生)[1] LI Hong-Jie(李红洁)[1]
HUANG Yan(黄彦)[1] ZHANG Yan(张嫣)[1] DUAN Li-Min(段利敏)[2] HU Rong-Jiang(胡荣江)[2]
LU Chen-Gui(鲁辰桂)[2] YANG He-Run(杨贺润)[2] MA Peng(马朋)[2]

[1] Department of Physics, Tsinghua University, Beijing 100084, China
[2] Institute of Modern Physics, Chinese Academy of Sciences, Lanzhou 730000, China
[3] Collaborative Innovation Center of Quantum Matter, Beijing 100084, China

Abstract: A prototype of the forward tracking array consisting of three multiwire drift chambers (MWDC) for the external target experiment (CEE) at the Heavy Ion Research Facility at the Lanzhou -Cooling Storage Ring (HIRFL-CSR) has been assembled and tested using cosmic rays. The signals from the anode wires are amplified and fed to a Flash-ADC to deliver the drift time and charge integration. The performances of the array prototype are investigated under various high voltages. For the tracking performances, after the space-time relation (STR) calibration and the detector displacement correction, the standard deviation of 223 μm of the residue is obtained. The performances of the forward MWDCs tracking array meets the requirements of CEE in design.

Key words: external target experiment, multiwire drift chamber, flash-ADC, tracking

PACS: 29.40.Gx, 29.85.Fj **DOI:** 10.1088/1674-1137/38/12/126002

1 Introduction

The phase diagram of strongly interacting matter is one of the scientific motivations for intermediate and high energy heavy ion collisions. In the region of low temperature and high net baryon density, the nuclear equation of state (EOS) is the key point to understand the phase diagram as well as the properties of stellar objects, the statical properties of nucleus and the collision dynamics [1]. The density dependence of the isovector part of the nuclear EOS, namely the symmetry energy, is one of the most unknown ingredients of the nuclear EOS, although great efforts have been made during the last decade both experimentally and theoretically [2]. Recently, the charged pion data published by FOPI collaboration [3] have been used to constrain the symmetry energy at suprasaturation densities within the framework of transport models, for which controversial conclusions on the stiffness of the symmetry energy are made [4–6]. Later a symmetry energy with different but moderate stiffness has been extracted from the differential elliptical flow of neutrons and hydrogen isotopes in Au+Au collisions [7]. Clearly more experimental and theoretical studies are necessary to arrive at a convincing conclusion. Recently, several modern worldwide experiments have been proposed to resolve the high density $E_{\rm sym}(\rho)$, including the differential nucleon elliptic flow with ANSYS-EOS [8], SAMURAI-TPC experiment [9] and the LAMPS experiment on RAON [10]. For a review, we refer to Ref. [11].

The Heavy Ion Research Facility at the Lanzhou, Cooling Storage Ring (HIRFL-CSR), started running recently and delivers heavy-ion beams up to 1 GeV/u. As demonstrated in Ref. [12], heavy ion collisions in this energy regime are favored for discriminating the effect of symmetry energy because the degree of isospin fractionation is large. While many detector researches and developments are ongoing for the physics programs at CSR [13–21], a CSR external target experiment (CEE) has also been proposed for the experimental studies on the asymmetric nuclear equation of state [22, 23].

The observables proposed for constraining the symmetry energy include charged pion ratio and t/^{3}He yield ratio, thus charged particle tracking is essential on CEE. Drift chambers have been widely used for charge particle tracking at many worldwide high energy experi-

Received 4 September 2014

∗ Supported by Natural Science Foundation of China (11079025, 11375094, U1332207) and Tsinghua University Initiative Scientific Research Program

1) E-mail: xiaozg@tsinghua.edu.cn

ments since its advent [24, 25] for their great advantages in low cost, large volume (size) and high performance. For instance, the BEjing Spectrometer (BES) at BEPC adopts a large volume main drift chamber with a tracking residue of better than 120 μm in beam test [26–28]. Two types of drift chambers are also applied in the design of CEE, a time projection chamber (TPC) and 6-planar multiwire drift chambers (MWDC), as shown in Fig. 1. The TPC is placed in a dipole with large acceptance for tracking the charged particles in midrapidity. Outside the TPC is a layer of multi-layer resistive plate counter (MRPC) to provide the time of flight (TOF) measurement. For the forward angle below 15° in laboratory reference, two arms of tracking array, each consisting of three pieces of planar MWDCs and one layer of MRPC, are installed in the downstream side of the dipole magnet to detect the charged particle tracks at large rapidity. A neutron wall is installed at zero degree to detect the neutrons produced in the reaction and offers a centrality selection.

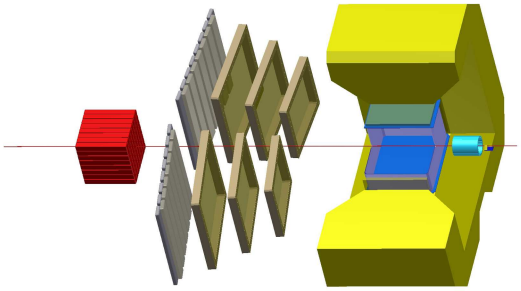

Fig. 1. (color online) The concept design of the CSR external target experiment (CEE).

In this paper, the first result of testing a prototype of the MWDC tracking system is reported. Section 2 presents the structural parameters of the prototype and the experimental setup. The calibration procedure and the main results are presented in Section 3. Section 4 is the outlook and summary.

2 Experimental setup

The prototype of the MWDC tracking system consists of three MWDCs installed in parallel between two scintillators, which provide the trigger for the cosmic ray event. The sensitive area of the chamber is 8 cm×8cm. The distance between the upper and middle chamber is 106 mm, while the middle-lower chamber distance is 86 mm. Each chamber has three sense layers called X, U and V respectively. Fig. 2 shows the layout and structure of the drift chamber in one direction (X-layer).

The X-layer is parallel to one side of the chamber, while the U-layer and V-layer are rotated with respect to the normal direction of the chamber plane by 30° and −30°, respectively. Only one layer of wires is used in each chamber in the current test. The U-layer and V-layer have the same structure. Each layer has a sense wire plane, extended in two parallel field wire planes. The distance between the two field wire planes is 10 mm and the inter field wire distance is 2 mm. On the sense wire plane, the sense wire and the field wire are stretched equidistantly next to each other. Thus around each sense wire, a drift cell of 10 mm×10 mm is formed by 12 field wires. A negative high voltage is fed on the field wires while the signals are extracted from the sense wire. The distance between two neighboring sense wires is 10 mm. The diameters of the field wire and the sense wire are 100 μm and 20 μm, respectively. The chambers are operated with a mixture of Ar(90%) and CO_2(10%) as the working gas at a flow of 40 mL/min. The signal from each sense wire is pre-amplified and then delivered to Flash-ADC for timing and charge integration. In the cosmic ray test, the start-trigger signal of the Flash-ADC is produced by the coincidence of the two scintillators.

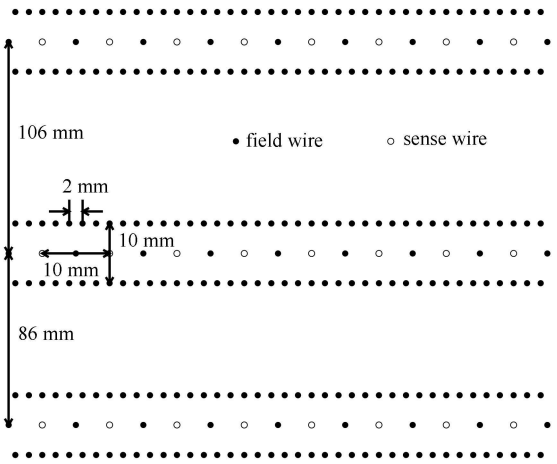

Fig. 2. (color online) Layout and structure of prototype (X-layer). This figure is not plotted in scale.

3 Results and discussions

3.1 Pulse processing: timing and charge integration

The signal from the sense wire is firstly amplified by a pre-amplifier, which is designed specifically for the drift chamber. The amplified signal is then delivered to a 250 MHz, 12 bit Flash-ADC module (CAEN V1720). The waveform is acquired and stored to disk without further online analysis. Then the pulse processing will be done offline to deduce the arrival time and the charge integration. During each trigger window, in total 128 sample points are acquired by the Flash-ADC module, and the interval between every sample point is 4 ns.

Figure 3 shows a typical waveform of the signal. The rising time and falling time are about 30 ns and 80 ns respectively. Considering the fast leading edge of the pulse, the arrival time of the pulse is determined by linear fitting of the leading edge. The fitting function has a form of $A=kt+b$, then the arrivial time is determined by:

$$t=-b/k. \tag{1}$$

The charge integration is done by adding the amplitude value of each sample point a_i directly. That is:

$$Q=\sum_i a_i. \tag{2}$$

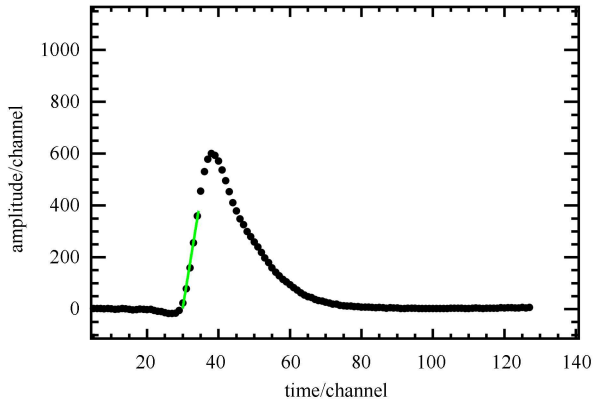

Fig. 3. (color online) A typical pulse from wire induced by a cosmic ray. The arrival time is determined by linear fitting of the leading edge, while energy loss is determined by integration of the pulse.

3.2 Determination of zero point of drift time distribution

We firstly investigate the feature of the inclusive drift distribution. Fig. 4(a) shows the amplitude-time scattering plot for one wire at 1700 V. Because of the method we used for timing, there is no correlation between amplitude and arrival time. Fig. 4(b) shows the amplitude distribution for a wire. The main peak of the distribution is contributed by the electrons drift from the main region of the cell, while the small amplitude events which have long drift time are due to the electrons drifting from the corner of the cell. Fig. 4(c) shows the drift time distribution of a cell. It is shown that there are roughly two components on the drift time distribution in accordance with the amplitude distribution. The main peak with a smaller drift time exhibits both left and right sharp edges corresponding to the events which leaves ionization in the main drift volume, while the tail with a larger drift time corresponds to the ionization that has taken place in the corner of the cell.

According to the method proposed in Ref. [29], the time distribution characterized by a sharp leading edge can be fitted with a function of:

$$N=B+A\frac{\mathrm{e}^{-t/\tau_1}}{1+\mathrm{e}^{(t-T_0)/\tau_2}}, \tag{3}$$

where T_0 is the zero point of the drift time distribution, which is the maximum point of the first derivative of the distribution. Then the real drift time T_d of each pulse for each wire can be derived by:

$$T_\mathrm{d}=t-T_0. \tag{4}$$

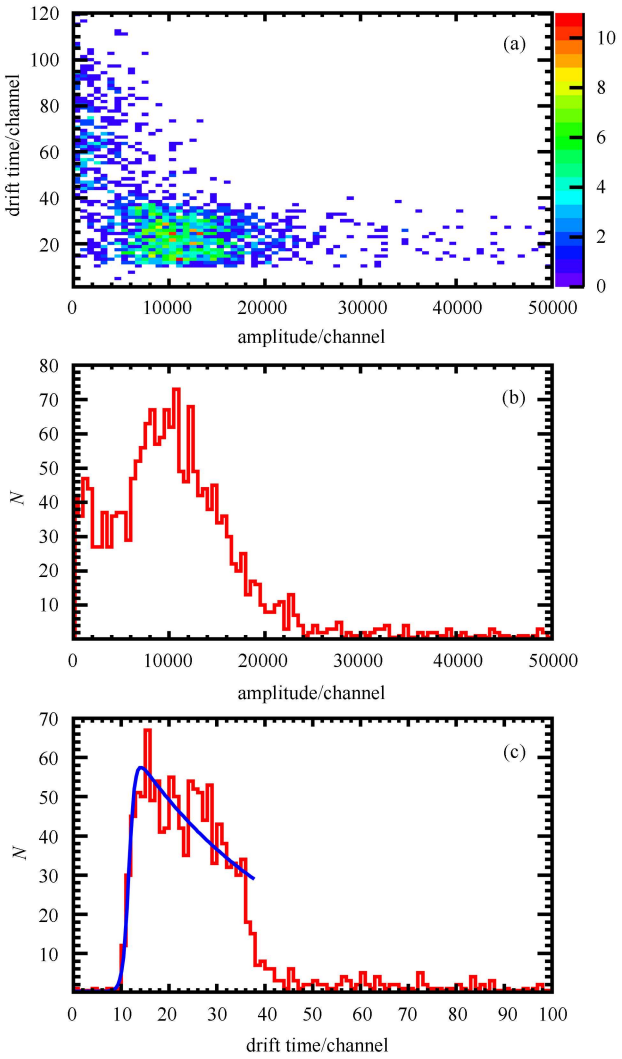

Fig. 4. (color online) (a) Amplitude-time scattering plot for one wire at 1700 V. (b) The amplitude distribution for a wire. (c) The drift time distribution for a wire and the fitting of the zero point.

3.3 Space-time relation (STR) and self-tracking

Before reconstructing the track of a cosmic ray, the space-time relation (STR) in a drift chamber has to be mapped to derive the ionization position left by the cosmic ray passing through. However, the STR cannot be obtained from direct measurement, so in the first run

of track reconstruction, the STR is initialized by the GARFIELD++ calculation [30]. After giving the parameters of the chamber, such as wires geometry, specifications of gas and electric field, the drift time of an electron can be obtained by the program. Since the GARFIELD++ program approximately computes the space-time relation, an iterative calibration procedure is needed, as adopted in Ref. [31].

The calibration is done by a self-tracking procedure. The drift distance d_i is used in the track reconstruction, while $d_i^{\rm fit}$ is defined as the drift distance calculated from the fitted track. Then the χ^2 of fitting for a track can be defined as:

$$\chi^2=\sum_i (d_i-d_i^{\rm fit})^2. \tag{5}$$

The fitting procedure is just finding a track which can minimize χ^2. Then the fitting residue $r_i=d_i-d_i^{\rm fit}$ is accumulated as a function of the drift time.

Figure 5 shows the profile value of the residue as a function of the drift time before and after the STR calibration. It is evident that before STR calibration, there is deviation at a long drift time region. Then this deviation is fitted using a 5th order polynomial, and added to the original STR calculated by GARFIELD++. After an iterative process, the new STR is obtained and the profile value of residue converges to the zero point in the whole drift time region. Fig. 6 shows the final STR compared with the experiment data.

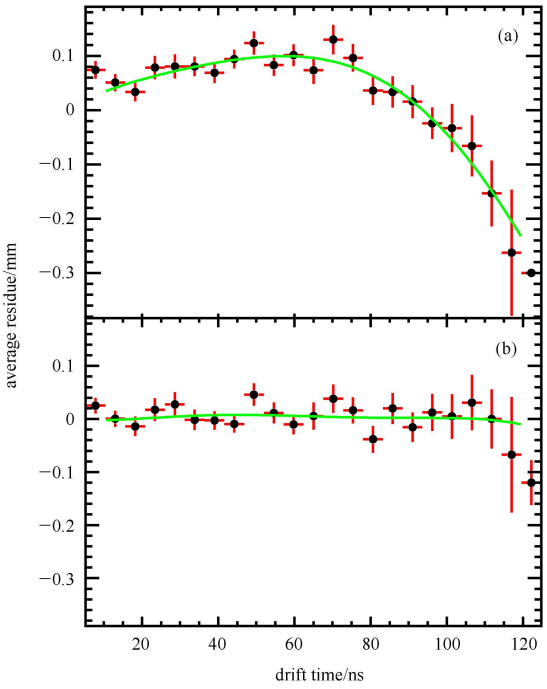

Fig. 5. (color online) The profile value of residue as a function of drift time before (a) and after (b) STR calibration.

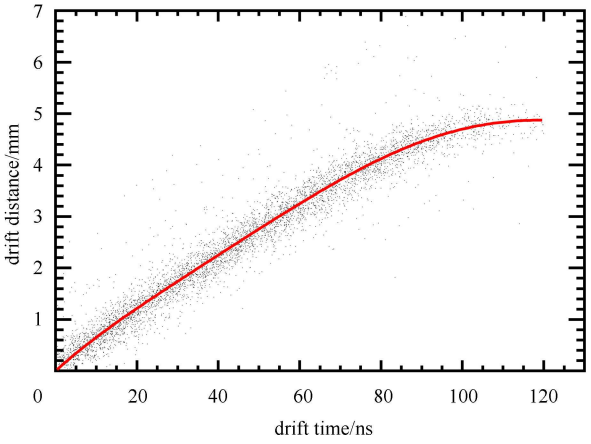

Fig. 6. (color online) Final STR after calibration, compared with the experimental data.

3.4 Horizontal displacement correction

Due to the random error in assembling the chambers, the relative displacement among different sense planes appears and may cause a system error in the track reconstruction result. So correction of the displacement between each chamber is necessary. For this, the horizontal coordinates of upper and lower chambers are adjusted in a certain interval with a step smaller than the required precision. For every adjusted displacement value, the track reconstruction procedure is done with calibrated STR. The residue distribution is fitted using a dual Gaussian function, as proposed in Ref. [27] and the standard deviation of the residue is evaluated as:

$$\sigma=\sqrt{\frac{N_1\sigma_1+N_2\sigma_2}{N_1+N_2}}, \tag{6}$$

where N_i and σ_i represent the net peak area and the standard deviation of each Gauss peak respectively. Fig. 7 shows the distribution of residue after correction at

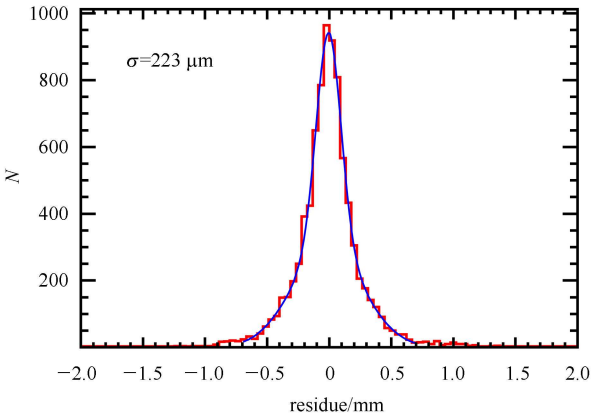

Fig. 7. (color online) Residue distribution after displacement correction and STR calibration at 1680 V.

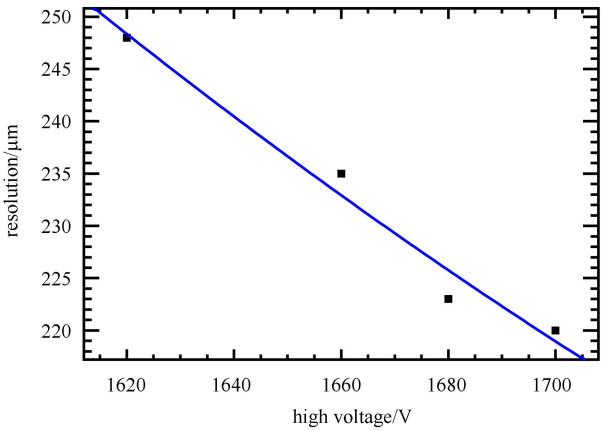

Fig. 8. (color online) Spatial resolution at different operating high voltages.

1680 V. The non-Gaussian tail in the residue distribution is due to the electrons which drift from the corner of the cell where the electric field has a distortion, so a non-isochronic behavior arises. While the correction value corresponds to the minimum value of σ, which is considered as the well-done displacement correction, and σ is treated as the spatial resolution of the chamber array.

3.5 Tracking resolution

After the horizontal displacement correction and STR calibration, the tracking procedure is finalized and the track residue is recalculated. the test was made by setting different voltages varying from 1620 V to 1700 V. The data analysis procedure keeps the same for all data analysis.

The spatial resolution as a function of the high voltage is shown in Fig. 8. It is shown that the residue is improved by about 15% if the voltage increases from 1620 V to 1680 V, at which the residue is about 223 μm. Above 1680 V, the improvement of the resolution is gradually saturated, meanwhile, the shape of the original signal from the wire starts to show distortion if the high voltage keeps increasing. At 1680 V, the track resolution can meet the requirement of the CEE experiment.

4 Summary

In summary, a prototype of the MWDC tracking array for the HIRFL-CSR external target experiment (CEE) is constructed and tested using cosmic rays. By careful STR calibration and horizontal displacement correction, the tracking residue distribution is measured at various high voltages. It is found that the resolution is improved largely with increasing the high voltage. At typical working voltage 1680 V, the standard deviation of the tracking residue of about 223 μm is achieved. The performance matches the requirement of the design of CEE.

References

1 Danielewicz P, Lacey R, Lynch W G. Science, 2002, **298**: 1592
2 LI B A, CHEN L W, Ko C M. Phys. Rep., 2008, **464**: 113
3 Reisdorf W et al. (FOPI collaboration). Nucl. Phys. A, 2007, **781**: 459
4 XIAO Z G, LI B A, CHEN L W et al. Phys. Rev. Lett., 2009, **102**: 062502
5 FENG Z Q, JIN G M. Physics Letters B, 2010, **683**: 140
6 XIE W J, ZHANG F S et al. Physics Letters B, 2013, **718**: 1510
7 Russotto P et al. Eur. Phys. J. A, 2014, **50**: 38
8 Russotto P et al. J. Phys. Conf. Ser., 2013, **420**: 012092
9 Kobayashi T et al. Nucl. Instrum. Methods B, 2013, **317**: 294
10 HONG B et al. Eur. Phys. J. A, 2014, **50**: 49
11 XIAO Z G et al. Eur. Phys. J. A, 2014, **50**: 37
12 ZHANG M, XIAO Z G et al. Phys. Rev. C, 2009, **80**: 034616
13 WU K J, LIU F. HEP & NP, 2007, **31**: 1022 (in Chinese)
14 WU K J et al. HEP & NP, 2007, **31**: 617 (in Chinese)
15 YUE K, XU H S et al. Chin. Phys. C, 2011, **35**: 67
16 YUE K, YU Y H et al. Chin. Phys. C, 2010, **34**: 1111
17 YU Y H et al. Chin. Phys. C, 2009, **33**: 557
18 YU Y H et al. Chin. Phys. C, 2009, **33**: 781
19 LIU D et al. Chin. Phys. C, 2010, **34**: 479
20 LU C G, DUAN L M et al. Chin. Phys. C, 2011, **35**: 1033
21 JI C S, SHAO M et al. Chin. Phys. C, 2013, **37**: 046201
22 XIAO Z G et al. J. Phys. G: Nucl. Part. Phys., 2009, **36**: 064040
23 ZHANG M, XIAO Z G et al. Chin. Phys. C, 2010, **34**: 1100
24 Charpak G, Sauli F. Nucl. Instrum. Methods, 1973, **107**: 371–373
25 Heintze J. Nucl. Instrum. Methods, 1978, **156**: 227–244
26 BESIII Collab., BESIII Preliminary Design Report, 2004, http://bes.ihep.ac.cn/bes3/design05/design/design1.htm
27 LIU J B et al. Nucl. Instrum. Methods A, 2006, **557**: 436
28 QIN Z H, CHEN Y B et al. Nucl. Instrum. Methods A, 2007, **571**: 612
29 Adinolft M et al. Nucl. Instrum. Methods A, 2002, **488**: 51
30 http://garfieldpp.web.cern.ch/garfieldpp/
31 Grossheim A, Hu J, Olin A. Nucl. Instrum. Methods A, 2010, **623**: 954